Measurement and theoretical simulation of the $HCCO^-$ anion photoelectron spectrum

Boris Schäfer-Bung
Institut für Physikalische und Theoretische Chemie, Universität Bonn, Wegelerstraße 12, D-53115 Bonn, Germany

Bernd Engels
Institut für Organische Chemie, Universität Würzburg, Am Hubland, D-97074 Würzburg, Germany

Travis R. Taylor and Daniel M. Neumark
Department of Chemistry, University of California, Berkeley, California 94720

Peter Botschwina
Institut für Physikalische Chemie, Universität Göttingen, Tammannstraße 6, D-37077 Göttingen, Germany

Miljenko Perić
University of Belgrade, Faculty of Physical Chemistry, Studentski trg 16, POB 137, 11001 Belgrade, Yugoslavia

(Received 22 March 2001; accepted 18 April 2001)

The photoelectron spectrum of $HCCO^-$ at the photodetachment wavelength of 355 nm is reported. A theoretical model for the simulation of the photodetachment process is described and the influence of various parameters is discussed. The experimental spectrum is compared with the simulation and an assignment of the spectrum is given. © *2001 American Institute of Physics.*
[DOI: 10.1063/1.1378041]

I. INTRODUCTION

The HCCO radical is of great interest in combustion chemistry because it is a key intermediate in the oxidation of small hydrocarbons such as acetylene. Spectroscopic information has been limited to a handful of experiments, none of which has adequately characterized the Renner–Teller interaction of the two lowest-lying electronic states. In this paper, theory recently developed to describe the Renner–Teller effect in tetra-atomics in combination with the Franck–Condon principle is used to compute the photoelectron spectrum of $HCCO^-$. The theoretical results are compared with a new photoelectron spectrum of $HCCO^-$ obtained at 355 nm (4.493 eV).

Rotational and vibrational spectroscopies have determined several properties of the ground state. From the submillimeter spectrum of HCCO, Endo *et al.*[1] were able to determine the geometry of the $X\,^2A''$ ground state. The anomalous K dependence of the spin–rotational splittings confirmed the presence of the close-lying Renner–Teller component. Ohshima *et al.*[2] further characterized the HCCO ground state by determining the hyperfine constants of the hydrogen nucleus using Fourier transform microwave spectroscopy. While performing experiments to elucidate the absorption spectroscopy of the C_2H radical, Jacox and Olson observed a transition at $2020\,cm^{-1}$ and attributed it to the HCCO radical. Several other transitions in their spectrum were not identified and may be attributed to the HCCO radical as well. Motivated by this finding, Curl and co-workers[3,4] confirmed this result in the gas phase via infrared flash kinetic spectroscopy and assigned it to the ν_2 stretching mode.

The $B\,^2\Pi$ excited state has been studied using photofragment translational spectroscopy and laser-induced fluorescence spectroscopy (LIF). Osborn *et al.*[5] investigated the $B\,^2\Pi \leftarrow X\,^2A''$ transition via photofragment translational spectroscopy and concluded that the excited state is Renner–Teller active. Brock *et al.*[6,7] have observed the same band via LIF. They were able to further characterize the spin–orbit components of the $B\,^2\Pi$ state and attributed a vibrational hotband of $494\,cm^{-1}$ to the ν_6 CCH bending mode. Finally, Oakes *et al.*[8] have taken low-resolution anion photoelectron spectra at 2.540 and 2.707 eV. At these energies they were able to observe five vibrational states of the neutral species. However, they were unable to make any spectral assignments. They report the electron affinity to be 2.350 ± 0.020 eV. Using this information with other thermodynamic values available in the literature, they are able to compute the heat of formation of the anion and neutral of HCCO.

The anion photoelectron spectrum reported here was taken at a photon energy of 3.493 eV, allowing us to observe many more transitions of the lowest-lying Renner–Teller pair. The resolution of our spectrum is high enough to allow adequate comparison with state of the art theory describing Renner–Teller effect in tetra-atomics.

The HCCO radical was also the topic of various theoretical studies. The geometrical structure of the ground state and of the first excited state was investigated by Goddard,[9] Kim and Shavitt,[10] Nguyen *et al.*,[11] and Szalay *et al.*[12,13] The equilibrium structure of the $X\,^2A''$ ground state was found to be *trans*-planar bent while a linear structure was predicted for the $A\,^2A'$ excited state. At linear geometry both states are degenerate, representing the two components of the corresponding $^2\Pi$ state. While most theoretical methods predict a *trans*-planar bent equilibrium structure for the $X\,^2A''$ state,

the explicit values of the geometrical parameters and the barrier to linearity strongly depend on the method of calculation and the AO basis set size. For example, the barrier to linearity shifts from $1302\,cm^{-1}$ [double zeta plus polarization (DZP)] to $643\,cm^{-1}$ [polarized valence triple zeta (PVTZ)] depending on the size of the AO basis set.[12,13]

Theoretical studies about the vibrational structure of HCCO were performed by Szalay *et al.*[12,13] and by Schäfer *et al.*[14] While Szalay *et al.* computed the vibrational spectra of the HCCO radical employing a harmonic ansatz, Schäfer *et al.*[14] calculated the lower-lying part of the rovibronic spectrum of HCCO including the Renner–Teller coupling between the two lowest-lying electronic states of HCCO and the anharmonic effects.

The potential energy surface of the $HCCO^-$ anion was investigated by Botschwina and co-workers.[15,16] In these calculations they found a *trans*-planar bent $X\,^1A'$ ground-state equilibrium geometry with rather low barrier height to linearity (not exceeding $300\,cm^{-1}$) and also determined the harmonic vibrational spectrum of the $HCCO^-$ anion. A more detailed discussion of the recent works studying the equilibrium geometries and the vibronic structures of both molecules will be given in connection with the new results.

In the present paper, the new experimental results are presented and an assignment of the spectrum is discussed. For the assignment of the spectrum we combine the theoretical data calculated for the neutral molecule and the anion and compute the relative intensities of the spectral bands. For the simulation we use a model which was recently developed to handle the Renner–Teller effect in tetra-atomic species. The article is organized as follows. The experiment and the resulting spectrum are described in Sec. II, while the calculations of equilibrium structures are given in Sec. III. After a brief discussion of the model employed for the simulation of the spectrum (Sec. IV), the influence of its parameters on the spectrum is analyzed, the spectrum is assigned, and our data are compared with previous results (Sec. V).

II. EXPERIMENT

The anion photoelectron spectrometer used in the present study has been described in detail previously.[17,18] In the current work, a mixture of 1% C_2H_2, 3% N_2O, and 6% O_2 in a balance of neon is expanded through a pulsed piezoelectric valve at a backing pressure of 40 psi. The resulting molecular beam passes through a pulsed electric discharge assembly,[19] creating a variety of anions. The flow supersonically expands and passes through a skimmer. The negative ions are extracted perpendicular to their flow direction by a pulsed electric field and injected into a linear reflectron time-of-flight (TOF) mass spectrometer[20,21] with a mass resolution $m/\Delta m$ of 2000. The ions of interest are selectively photodetached with photons having wavelengths of 355 nm (3.493 eV). The 355 nm wavelength is obtained by frequency tripling the fundamental of a pulsed Nd:YAG laser. The electron kinetic energy (eKE) distribution is determined by TOF analysis in a 1 m field-free flight tube. The energy resolution is 8 meV at eKE of 0.65 eV and degrades as $(eKE)^{3/2}$ at higher eKE.

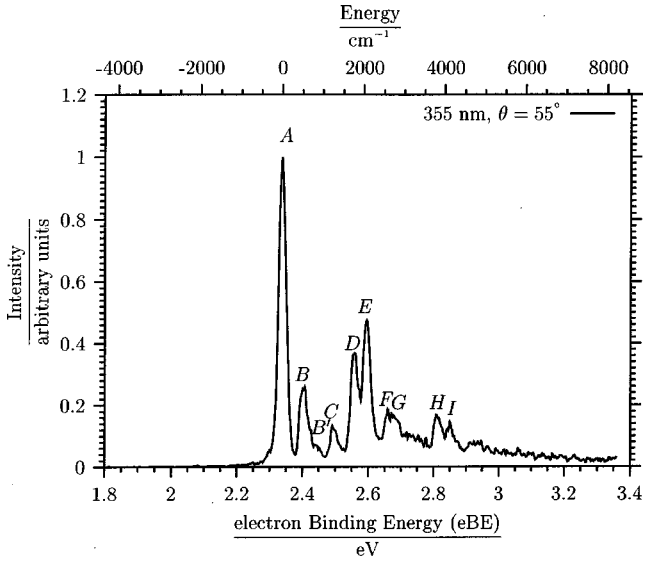

FIG. 1. Photoelectron spectrum of $HCCO^-$ taken at a photon wavelength of 355 nm and at magic polarization angle. The lower abscissa reports the electron binding energy eBE, the upper abscissa denotes energy in wave numbers where peak *A* represents the origin.

Figure 1 shows the photoelectron spectrum of $HCCO^-$ taken at 355 nm. The bottom axis of the photoelectron spectrum is reported in electron binding energy, eBE, which is defined as $eBE = h\nu - eKE$. The top axis of the spectrum shows the energy scale in wave numbers with peak *A* chosen as the reference point. A spectrum taken at a higher detachment wavelength (416 nm) showed only minor differences and is not included in this paper. The photoelectron differential cross section[22] is given by

$$\frac{d\sigma}{d\Omega} = \frac{\sigma_{\text{total}}}{4\pi}\left[1 + \frac{\beta(E)}{2}(3\cos^2\theta - 1)\right]. \tag{1}$$

The polarization angle, θ, is the angle between the electric vector of the photon and the axis along which the electrons are detected. The differential cross section is parametrized in terms of the anisotropy parameter, β, with $-1 \leqslant \beta \leqslant 2$. The anisotropy parameter for a particular peak is obtained from the relative peak intensities taken at different polarization angles. Peaks with differing values of β generally result from transitions to different neutral electronic states, so this can be used to assign electronic states and to distinguish contributions from overlapping electronic bands. Spectra were taken at polarization angles of 0, 55°, and 90°. All peaks in the spectrum show the same polarization dependence, yielding a β parameter of -0.18 ± 0.06.

The features in Fig. 1 are labeled as peaks *A* to *I*. The peak located at the lowest electron binding energy, peak *A*, is the most intense feature in the spectrum. At electron binding energies higher than that of peak *I* there is a low intensity background extending to the end of the spectrum. This low-intensity unresolved feature also extends toward lower electron binding energies and accounts for the fact that the baseline is not visible on the right-hand side of peak *A*.

Taking peak *A* as the transition between $\nu = 0$ levels of the $HCCO^-$ and HCCO ground states yields an electron affinity of 2.338 ± 0.008 eV, in agreement with the previously obtained result[8] of 2.350 ± 0.020 eV. The remaining peaks *B*

TABLE I. Equilibrium geometries (bond lengths in Å, angles in °) and total energies (in E_h) for trans-$HCCO^-$.

Method	Correlated electrons	AO basis set	N_{cGTO}	r_{OC}	r_{CC}	r_{CH}	ρ_1	ρ_2	V_e
CEPA-1	all	aug-cc-pVTZ[a]	151	1.2192	1.2591	1.0676	7.5	41.6	
CCSD(T)	all	aug-cc-pVTZ[a]	151	1.2226	1.2635	1.0694	7.9	41.1	
CCSD(T)	val	aug-cc-pVTZ	161	1.2279	1.2711	1.0724	8.4	43.4	−151.775 070
CCSD(T)	val	aug-cc-pVQZ	286	1.2249	1.2664	1.0709	8.1	42.1	−151.813 815
CCSD(T)	all	aug-cc-pCVQZ	352	1.2224	1.2635	1.0695	7.9	41.5	−151.982 187

[a]Exclusive of *d* functions at hydrogen (Refs. 15 and 16).

to *I* represent transitions to excited vibrational levels of HCCO. These features are considerably better resolved than in the previous study by Oakes *et al.*,[8] thereby facilitating a detailed comparison with the theoretical simulations of the photoelectron spectrum described in the following sections.

III. ACCURATE EQUILIBRIUM STRUCTURES AND BARRIERS TO LINEARITY FOR $HCCO^-$ AND HCCO

Since the rovibrational or rovibronic structure of a photoelectron spectrum is mainly determined by the changes in the equilibrium geometries of the corresponding *N* and $(N-1)$ electron systems, we have carried out extensive geometry optimizations for $HCCO^-$ and HCCO. The MOLPRO98[23] suite of programs was used in these calculations. For the anion, basis sets as large as 352 contracted Gaussian type-orbitals (cGTOs) were employed in conjunction with the coupled-cluster method with single and double excitations and perturbative triple corrections [CCSD(T)].

Results of the calculations for trans-$HCCO^-$ are listed in Table I, which also includes data from earlier calculations.[15,16] The largest basis employed, termed aug-cc-pCVQZ, corresponds to the correlation-consistent polarized core-valence quadruple zeta basis of Woon and Dunning,[24] which was augmented by diffuse *s*, *p*, *d*, *f*, and *g* functions for carbon and oxygen and by diffuse *s*, *p*, *d*, and *f* functions for hydrogen.[25] All electrons were correlated in the CCSD(T) calculations with this basis. The smaller basis sets of 161 and 286 cGTOs are the aug-cc-pVTZ and aug-cc-pVQZ sets of the Dunning group. The equilibrium bond lengths obtained by CCSD(T)/all with the largest basis are expected to be accurate to 0.001 Å; the errors in the equilibrium bond angles should not exceed a few tenths of a degree. Somewhat fortuitously, our older CCSD(T) results[15,16] are almost identical due to the effects of error compensation. Optimum geometrical parameters for linear $HCCO^-$ and barrier heights to linearity as obtained from five different types of calculations are listed in Table II. Compared to *trans*-$HCCO^-$, the C–H and C–C bond lengths are shortened by 0.0110 Å and 0.0226 Å, respectively, while the C–O bond length is elongated by 0.0091 Å (CCSD(T)/all; 352 cGTOs). The calculated barrier height to linearity shows a significant variation with the size of the basis set. Our earlier calculations with the almost complete aug-cc-pVTZ basis, in which all electrons were correlated, yielded barrier heights of 227 and 272 cm^{-1} at the CEPA-1 and CCSD(T) level, respectively. Using the full aug-cc-pVTZ basis and correlating only the valence electrons, what one usually should do with this basis, a higher barrier height value of 523 cm^{-1} is obtained at the CCSD(T) level. Extension of the basis set to aug-cc-pVQZ (286 cGTOs) reduces the barrier height to linearity to 428 cm^{-1}, while inclusion of core–valence and core–core correlation in conjunction with the addition of suitable basis functions (aug-cc-pCVQZ) leads to a further reduction to 385 cm^{-1}, which constitutes our most reliable value.

Results for *trans*-HCCO, the lower component of the Renner–Teller system, and for linear HCCO are given in Tables III and IV. The open-shell coupled-cluster variant employed in this work is termed RHF-UCCSD(T), which indicates that a restricted Hartree–Fock determinant was used as a reference wave function and that the unrestricted coupled-cluster formalism was used to describe electron correlation effects (see Refs. 26 and 27 for details). Our best equilibrium structure estimate for *trans*-HCCO ($\tilde{X}\,^2A''$) was obtained in RHF-UCCSD(T) calculations with the cc-pCVQZ basis (282 cGTOs) in which all electrons were correlated (see the last line of Table III). Similar to the results obtained for $HCCO^-$, the calculations with the cc-pVTZ basis and all electrons correlated—either at the UHF-CCSD(T) level (Ref. 13) or at RHF-UCCSD(T) from this work—yield very similar results for the heavy-atom skeleton while the C–H equilibrium bond length is underestimated by almost 0.005 Å.

Our most reliable value for the barrier height to linearity

TABLE II. Optimum geometrical parameters (in Å), total energies (in E_h), and barrier heights (in cm^{-1}) for linear $HCCO^-$.

Method	Correlated electrons	AO basis set	N_{cGTO}	r_{OC}	r_{CC}	r_{CH}	V_e	Barrier height
CEPA-1	all	aug-cc-pVTZ[a]	151	1.2283	1.2375	1.0581		227
CCSD(T)	all	aug-cc-pVTZ[a]	151	1.2310	1.2426	1.0600		272
CCSD(T)	val	aug-cc-pVTZ	161	1.2376	1.2468	1.0602	−151.772 686	523
CCSD(T)	val	aug-cc-pVQZ	286	1.2338	1.2437	1.0598	−151.811 864	428
CCSD(T)	all	aug-cc-pCVQZ	352	1.2315	1.2409	1.0585	−151.980 433	385

[a]Exclusive of *d* functions at hydrogen (Refs. 15 and 16).

TABLE III. Equilibrium geometries (bond lengths in Å, angles in °) and total energies (in E_h) for *trans*-HCCO ($\tilde{X}\,^2A''$).

Method	Correlated electrons	AO basis set	N_{cGTO}	r_{OC}	r_{CC}	r_{CH}	ρ_1	ρ_2	V_e
RCCSD(T)[a]	val	DZP	50	1.1715	1.3310	1.0787	13.1	51.9	−151.537 925
UMP2[b]		TZP	66	1.167	1.314	1.071	10.1	51.8	
UHF-CCSD(T)[c]	all	cc-pVTZ	104	1.1728	1.2972	1.0660	10.6	45.4	−151.723 749
RHF-UCCSD(T)	val	cc-pVTZ	104	1.1760	1.3072	1.0738	11.7	48.1	−151.681 278
RHF-UCCSD(T)	all	cc-pVTZ	104	1.1742	1.2962	1.0658	10.5	44.9	−151.724 048
RHF-UCCSD(T)	val	aug-cc-pVTZ	161	1.1764	1.3080	1.0748	11.5	48.3	−151.691 494
RHF-UCCSD(T)	val	cc-pVQZ	195	1.1725	1.3031	1.0729	11.1	47.3	−151.724 907
RHF-UCCSD(T)	all	cc-pCVQZ	282	1.1710	1.2975	1.0709	10.7	45.9	−151.895 655

[a]Reference 14.
[b]Reference 12.
[c]Reference 13.

of the radical (cf. Table IV) is $637\,cm^{-1}$, obtained by RHF-UCCSD(T)/all with the basis of 282 cGTOs. Core–valence and core–core correlation make a contribution of $-75\,cm^{-1}$ to the barrier height. This contribution is grossly overestimated when the cc-pVTZ basis set is used (see the second and third lines of Table IV) with the result that, rather fortuitously, the earlier calculations at the UHF-CCSD(T)/all level[13] and the present RHF-UCCSD(T)/all calculations yield excellent agreement with the best value for the barrier height from this work.

Our best equilibrium structures for $HCCO^-$ and the lower Renner–Teller component of HCCO are graphically displayed in Fig. 2. Upon electron detachment, the equilibrium bond angles experience changes of less than 5° and the C–H equilibrium bond length remains practically unchanged. The C–C equilibrium bond length (r_{CC}) is increased by 0.034 Å and r_{CO} is reduced by 0.051 Å. On the whole, the change in equilibrum structures is fairly small so that the adiabatic peak should dominate the photoelectron spectrum and relatively little vibrational excitation should be observable.

IV. DESCRIPTION OF THE THEORETICAL MODEL

An *ab initio* simulation of the photodetachment spectrum of $HCCO^-$ is difficult due to various reasons. From the experience of our previous work on HCCO,[14] at least six nuclear degrees of freedom, i.e., the two bending vibrations, the torsion, the O–C and the C–C stretching motion, and the rotation around the axis corresponding to the smallest moment of inertia ($=a$ axis) and their mutual couplings have to be taken into account. Only the C–H stretching motion can safely be decoupled. Furthermore, since the neutral molecule and its negative ion represent quasilinear molecules, their vibronic structure is strongly influenced by anharmonic effects and large amplitude motions. Finally, the strong vibronic Renner–Teller coupling between the two lowest-lying electronic states of the HCCO has to be taken into account.

These considerations imply that for a rigorous treatment of the rovibrational resolved photodetachment spectrum of $HCCO^-$, a five-dimensional potential energy surface for the ground state of the anion and for both involved electronic states of the neutral molecule ($X\,^2A''$, $A\,^2A'$) would be necessary. These potential energy surfaces had to be computed with very sophisticated theoretical methods, bearing in mind the strong dependency of the potential energy surfaces on the method of calculation.[12,13] Due to the Renner–Teller effect the $X\,^2A''$ and the $A\,^2A'$ state of the neutral molecule had to be coupled and finally the high-dimensional nuclear Schrödinger equation had to be solved.

Nevertheless, as we will show in the present paper, an understanding of the spectrum is already possible using a simpler model, developed recently to describe the Renner–Teller effect in quasilinear tetra-atomic species.[14,28] The model exploits the fact that the coupling strengths between the various nuclear degrees of freedom differ considerably from each other. The differences arise from the energetical order of the vibrations and/or due to the size of the coupling matrix elements. Consequently, only the four nuclear degrees of freedom, which are involved in the Renner–Teller effect (i.e., the two bending modes, the torsion, and the rotation around the a axis) are handled explicitly in the model. The

TABLE IV. Optimum geometrical parameters (in Å), total energies (in E_h), and barrier heights (in cm^{-1}) for linear HCCO.

Method	Correlated electrons	AO basis set	N_{cGTO}	r_{OC}	r_{CC}	r_{CH}	V_e	Barrier height
UHF-CCSD(T)[a]	all	cc-pVTZ	104	1.1847	1.2609	1.0560	−151.720 818	643
RHF-UCCSD(T)	val	cc-pVTZ	104	1.1895	1.2653	1.0617	−151.677 673	791
RHF-UCCSD(T)	all	cc-pVTZ	104	1.1861	1.2606	1.0561	−151.721 196	626
RHF-UCCSD(T)	val	aug-cc-pVTZ	161	1.1901	1.2659	1.0625	−151.687 805	810
RHF-UCCSD(T)	val	cc-pVQZ	195	1.1856	1.2628	1.0616	−151.721 663	712
RHF-UCCSD(T)	val	aug-cc-pVQZ	286	1.1861	1.2631	1.0619	−151.725 502	
RHF-UCCSD(T)	all	cc-pCVQZ	282	1.1834	1.2600	1.0604	−151.892 751	637

[a]Reference 13.

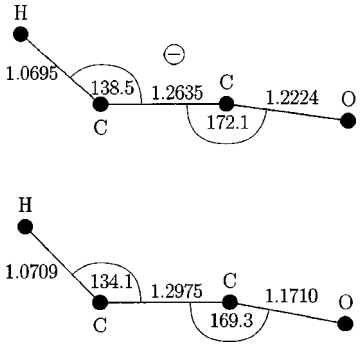

FIG. 2. Best equilibrium structures for HCCO$^-$ and HCCO (bond lengths in Å and bond angles in °).

coupling of these vibrations with the O–C and C–C stretching vibrations, characterized by appreciably higher vibrational frequencies, is taken into account indirectly by employing the idea developed by Bunker and Landsberg.[29,30] According to this approach, the leading part of the stretch–bend interaction is incorporated into the bending problem via a proper correction of the bending potential.

Excitations into vibrationally excited states of the O–C and C–C stretching vibrations of HCCO are anticipated to contribute only to the higher frequency range of the spectrum. Due to the fact that in the observed spectral region only few quanta of these vibrations can be excited, such vibrations can reasonably be treated in the harmonic approximation. The influence of the coupling of these two stretching vibrations on the spectrum is simulated using a one-dimensional and a two-dimensional ansatz.

The C–H stretching mode possessing a frequency around 3350 cm^{-1} does not significantly couple with other degrees of freedom, and thus was completely decoupled from the rest. Nevertheless, transitions into different states of the C–H mode were taken into consideration.

Using the model discussed above, the total wave function (nuclear and electronic part) factorizes into

$$\Psi(\mathbf{r},\mathbf{q}) = \psi_{\mathrm{el}}(\mathbf{r}) \cdot \chi_{\mathrm{CH}}(r_{\mathrm{CH}}) \cdot \chi_{\mathrm{OC,CC}}(r_{\mathrm{OC}}, r_{\mathrm{CC}}) \cdot \chi_{\mathrm{b}}(\rho_1, \rho_2, \varphi_1, \varphi_2), \tag{2}$$

whereby ψ_{el} represents the electronic wave function, χ_{CH} the wave function for the C–H stretching vibration, $\chi_{\mathrm{OC,CC}}$ the wave function for the mutually coupled O–C and C–C stretching vibrations, and χ_{b} the wave function for the bending modes. The wave function χ_{b} involves both the bending coordinates ($\rho_1 = 180° - \angle$ O–C–C, $\rho_2 = 180° - \angle$ C–C–H) and the two rotational coordinates φ_1 and φ_2. φ_1 describes the angle between the plane given by the O–C–C moiety and a space-fixed plane including the C–C axis, while φ_2 represents the corresponding angle for the C–C–H fragment. That means that φ_1 and φ_2 describe the movement of both terminal atoms around the C–C axis, which is assumed to coincide with the *a* axis. In the framework of our model, we assume that the projection of the total angular momentum (excluding spin) onto the *a* axis is conserved and thus the corresponding quantum number K is a good one. It is composed from the electronic quantum number Λ and the quantum number l for the projection of the nuclear angular momentum onto the *a* axis,[14,28]

$$K = |l + \Lambda| = |l_1 + l_2 + \Lambda|, \tag{3}$$

whereby l_1 and l_2 are the quantum numbers corresponding to the coordinates φ_1 and φ_2 and all quantum numbers l_1, l_2, and Λ are assumed to be signed quantities.

For the simulation of the relative intensities I of the photodetachment spectra of HCCO$^-$ the generally accepted Franck–Condon approximation is employed[31–33]

$$I \sim |\langle \chi^\circ | \chi^- \rangle|^2, \tag{4}$$

i.e., we assume that the electronic part of the transition probability is constant and does not differ substantially for the two considered electronic states of HCCO. In Eq. (4) the $^-$ and the $^\circ$ superscripts denote the wave functions of the anion and of the neutral system, respectively. For the model described above, the Franck–Condon factor f factorizes as

$$f = f_{\mathrm{CH}} \cdot f_{\mathrm{OC,CC}} \cdot f_{\mathrm{b}}. \tag{5}$$

Within this Franck–Condon approach, for transitions from the negative ion to the neutral molecule the projection of the nuclear angular momentum onto the *a* axis is conserved throughout the photodetachment process. The corresponding quantum numbers obey $l^- = l^\circ$, which in turn leads to $K^- = K^\circ \pm 1$ for the K quantum numbers.[34,35] The Franck–Condon factor f_{b} is obtained by calculating the square of the norm of the overlap integral of the bending wave functions $\chi_{\mathrm{b}}^{\circ}$ and χ_{b}^{-}. These functions, which are provided by calculations of the rovibronic spectra of HCCO$^-$ and HCCO (both given below), are represented in the same rovibrational basis set.[28] The Franck–Condon factors f_{CH} and $f_{\mathrm{OC,CC}}$ are determined, respectively, by means of one-dimensional and two-dimensional standard harmonic oscillator wave functions.

In experiments the vibrational temperature of the anion was estimated to be about 200 K. The influence of the temperature on the spectra was simulated under the assumption that the anion energy levels are occupied according to a Boltzmann distribution. The Franck–Condon factors were weighted by the corresponding Boltzmann factors.

Finally, the finite experimental resolution was simulated by broadening the theoretical stick spectrum by means of a Gaussian distribution. The energy dependence of the resolution was taken from Eq. (2) of Ref. 18.

The shape of the potential energy surface (equilibrium geometry, barrier to linearity) of the $X\,^2A''$ ground state of HCCO, as already mentioned, strongly depends on the method of calculation and the AO basis-set size. Since the computation of all involved potential energy surfaces with an accuracy of a few wave numbers is not feasible, we modeled the shape of the potential energy surface using the previous theoretical results.[10,13,14] A scaled potential energy surface $\tilde{V}$ could be obtained from the previously computed overall potential V given in Fig. 3 of Ref. 14, using

$$\tilde{V}(\rho_1, \rho_2) := s_0 \cdot V(\overline{\rho_1}, \overline{\rho_2}) \quad \text{with} \quad \rho_i = s_i \cdot \overline{\rho_i}, \quad i = 1,2. \tag{6}$$

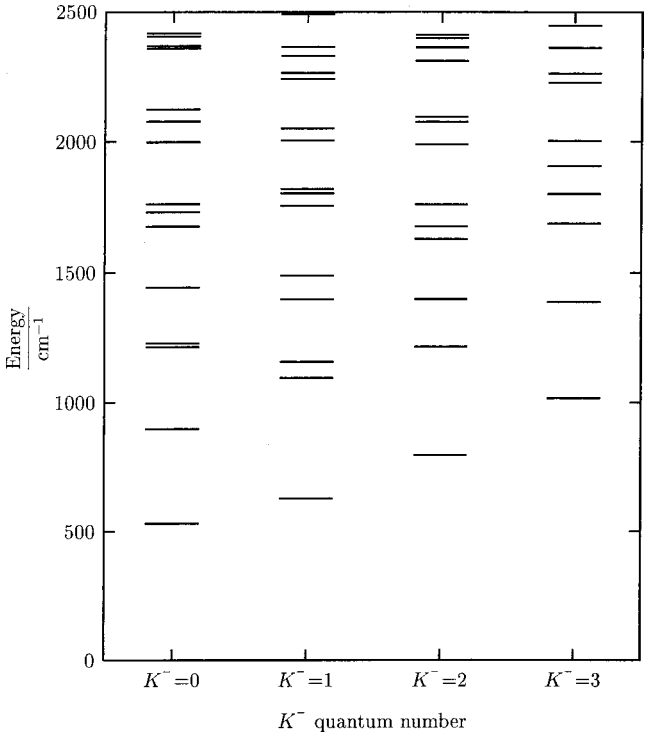

FIG. 3. Low-lying vibronic energy levels of the $X\,^1A'$ electronic state of $HCCO^-$ with respect to the quantum number $K^-=|l_1^-+l_2^-|$. The origin of the energy scale denotes the energy of the linear geometry.

To study the influence of the shape of the potential energy surface on the simulated photodetachment spectrum, the scaling factors s_0, s_1, and s_2 are chosen in such a way that potential surfaces with various barrier heights and equilibrium geometries can be created. The vibronic energy levels were computed for the various scaled potential energy surfaces employing the method presented previously. This approach seems to be reasonable considering the various assumptions made in our model (e.g., the Franck–Condon approximation, and the partial decoupling of the stretching from the bending vibrations).

In the present computations of the rovibrational spectrum of $HCCO^-$, the five-dimensional CEPA-1 surface[15] depending on two bending coordinates (ρ_1, ρ_2) and three stretching coordinates (r_{CC}, r_{CH}, and r_{OC}) is projected onto a three-dimensional section by relaxing all the stretching coordinates, and by representing the dependence of the potential on the torsional angle $\gamma=\varphi_1-\varphi_2$ by a simple cosine γ expression. This approach is very similar to the one we used earlier in our work.[14]

The bending vibrational levels for the $X\,^1A'$ ground state of $HCCO^-$ are also obtained by means of the program package described earlier.[14,28]

V. RESULTS AND DISCUSSION

The bending wave functions as well as the term values of the rovibrational spectrum of $HCCO^-$ and the rovibronic spectrum of HCCO are necessary for a computation of the $HCCO^-$ photodetachment spectrum. Hence, some details of the calculated vibronic spectra are given in the following paragraph. The low-lying part of the spectrum and the influence of the bending modes on this region of the spectrum are investigated in the succeeding three paragraphs. An assignment for this spectral range is performed. Then, the stretching modes are added and the remaining part of the spectrum is taken under consideration.

TABLE V. Low–lying vibronic levels of the $X\,^1A'$ electronic state of $HCCO^-$ for the quantum number $K^-=|l_1^-+l_2^-|=0,\ldots,3$. Term values $E_{K^-,i}$ are given in cm^{-1} with respect to the energy of the linear geometry. The first index of the quantity E reflects the K^- quantum number of the energy level; the level number i which is the second index of E indicates the energetical order beginning with the lowest value for the quantum number K.

Level number i	$K^-=0$ $E_{K^-=0,i}$	$K^-=1$ $E_{K^-=1,i}$	$K^-=2$ $E_{K^-=2,i}$	$K^-=3$ $E_{K^-=3,i}$
1	531	630	797	1017
2	898	1096	1215	1387
3	1214	1157	1398	1689
4	1228	1398	1629	1802
5	1443	1489	1677	1908
6	1677	1756	1761	2004
7	1732	1804	1989	2227
8	1763	1820	2075	2262
9	1997	2005	2094	2362
10	1998	2049	2311	2447
11	2077	2241	2363	
12	2124	2264	2399	
13	2360	2330	2412	
14	2369	2365		
15	2406	2492		
16	2417			

The results for the bending vibrational levels in the ground electronic state of $HCCO^-$ are given in Fig. 3 and Table V. Aside from the reduction of the dimensionality, as mentioned in the previous section, no scaling was applied to the potential energy surface of $HCCO^-$. The overall structure of this spectrum is typical for a quasilinear tetra-atomic molecule. Due to the fact that the barrier height to linearity is lower for $HCCO^-$ than for the neutral species, and because of different equilibrium geometries of HCCO and its anion (Tables I and III), the following differences occur in comparison to the rovibronic spectrum of the two lowest-lying states of the neutral molecule (Fig. 6 of Ref. 14):

(1) The spectrum is shifted towards higher energies if the origin of the energy scale denotes in both cases the energy of the linear geometry.
(2) From the K^--rotational ladder a value of the rotational constant of $(2I)^{-1}=99\,\mathrm{cm}^{-1}$ could be determined which exceeds the corresponding value in the case of HCCO more than three times.
(3) As shown in our earlier paper,[14] basic features of the low-energy range of the spectrum of HCCO can be reflected in the simplified model which represents two uncoupled triatomics, one with linear and the other with bent equilibrium geometry (Fig. 7 of Ref. 14). This is still valid in the present case. The values of $\omega_b=367\,\mathrm{cm}^{-1}$ $(E_{K^-=0,2}-E_{K^-=0,1})$ and $\omega_l=565\,\mathrm{cm}^{-1}$ $(E_{K^-=1,2}-E_{K^-=0,1})$, derived from the rovibrational spectrum by means of the simplified model, fit to the values given by the harmonic approximation (402 and

TABLE VI. Boltzmann factors for the low-lying levels of $HCCO^-$. Energy values are given in cm^{-1}. For explanation of the level number i and term value $E_{K^-,i}$, see Table V or the text.

Level number i	K^- quantum number	Term value $E_{K^-,i}$	Boltzmann factor
1	0	531	1.0000
1	1	630	0.4916
1	2	797	0.1475
2	0	898	0.0711

591 cm^{-1}, respectively). But, compared with the spectrum of HCCO, the anion spectrum can be understood as an intermediate between the simplified model described above and a simplified model which contains two uncoupled triatomics with linear equilibrium geometry. This is mainly caused by the enlarged rotational constant.

Further details are given in Ref. 36. The Boltzmann factors are calculated for the low-energy spectral range with respect to the lowest-lying level by assuming a rovibrational temperature of 200 K. They are given in Table VI. In the following we consider Franck–Condon factors for transitions from initial states which are labeled by $E_{K^-,1}$ (with $K^-=0,1,2$). Only for these states is the corresponding Boltzmann factor high enough to induce a non-negligible contribution to the spectrum. The second index of the quantity E is called here level number and labels the energetical order beginning with the lowest value for each quantum number K.

In order to enable a comparison between the experimental and the simulated spectrum, the latter is shifted along the energy axis and scaled along the intensity axis in such a way that the maximum of the most intense peak (=peak 0) coincides with the experimental peak A.

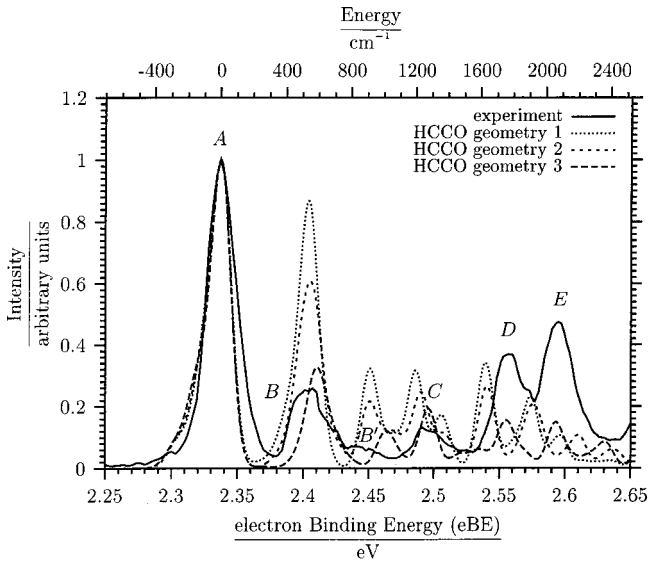

FIG. 4. Gaussian-broadened stick spectra for the fixed barrier height of 981 cm^{-1} and various equilibrium geometries of HCCO are compared with experimental results. The used equilbrium structures of HCCO are given in Table III.

For the structure of the photoelectron spectrum the relative location of both equilibrium geometries (HCCO and $HCCO^-$) with respect to each other plays an important role. Regarding the bending coordinates, for $HCCO^-$ the *trans*-planar equilibrium geometry of the CEPA–1 calculation (see the first row of Table I) with $\rho_1=7.5°$ and $\rho_2=41.6°$ is used. Due to small deviations of these coordinates from the values of the most reliable calculation (see the fifth row of Table I), the scaling of the geometry is omitted. Additionally, we found that for the anion even an appreciable difference of the barrier height could influence neither the difference of the important term values nor the character of the corresponding bending wave functions. For this reason the potential surface for the anions remains unscaled.

For the neutral species three geometries are considered:

(1st) Geometry: $\rho_1=13.1°$ and $\rho_2=51.9°$ of our RCCSD(T)/DZP calculation[14] (see the first row of Table III);

(2nd) Geometry: $\rho_1=10.1°$ and $\rho_2=51.8°$ of the UMP2/TZP calculation of Kim and Shavitt[12] (see the second row of Table III); and

(3rd) Geometry: $\rho_1=10.6°$ and $\rho_2=45.4°$ of UHF-CCSD(T)/cc-pVTZ calculation of Szalay *et al.*[13] (see the third row of Table III).

Considering the methods of calculation and the size of the AO basis sets, the third geometry is expected to give the best agreement between theory and experiment. In the following we will use the experimental spectrum for a refinement of the equilibrium geometry and of the height of the barrier to linearity of HCCO (the corresponding values for $HCCO^-$ are kept fixed). As an indicator for the coincidence, we focus on the congruence of the first peak (=peak 1) on the right-hand side of the reference peak in the simulation with the experimental peak B. In Fig. 4 the Gaussian-broadened stick spectrum for a fixed barrier height of 981 cm^{-1} (HCCO) is given for each of the three HCCO equilibrium geometries and compared with the experimental result. The intensity of peak 1 varies strongly with both bending coordinates. The more linear the equilibrium geometry, the smaller the intensity of peak 1. The best agreement with experimental intensity is obtained for the most linear geometry of HCCO (third geometry). Considering the location of that peak, only a change of the coordinate ρ_2 seems to be important and the second geometry fits better. For most of the other peaks displayed in Fig. 4 the statements given above remain valid. As expected, the geometry influences the intensity as well as the location of the peaks. The shift of the peak location is caused by the dependence of the HCCO term values and of the intensity contribution of transitions into the corresponding states from the equilibrium geometry. On the one hand, the shift of the peak location is caused by the dependence of the HCCO term values from the equilibrium geometry. On the other hand, changes of the intensity contribution of the various transitions belonging to one peak also influence the location of the maximum of the whole peak.

As seen before,[14] the height of the barrier to linearity also has a considerable impact on the spectrum. In order to investigate this effect, the barrier height is varied for fixed equilibrium geometry (the most linear geometry of HCCO

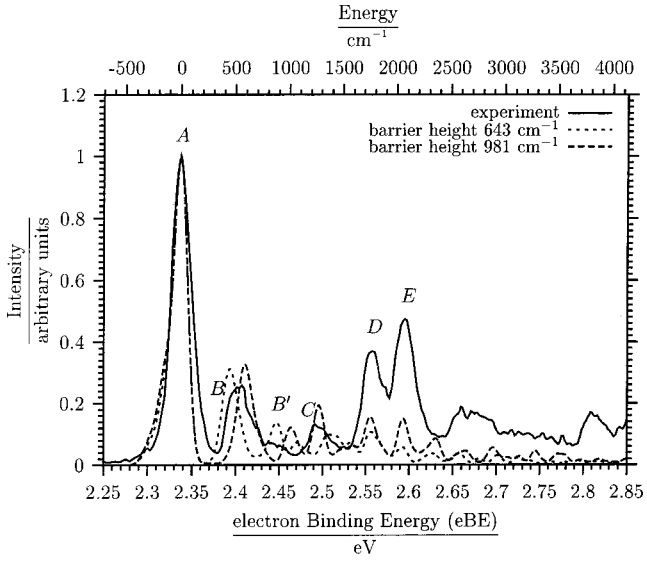

FIG. 5. Gaussian-broadened stick spectrum for the third geometry with different barrier heights along with the experimental spectrum.

was chosen). In Fig. 5 the calculated Gaussian-broadened spectrum with barrier heights of 643 and 981 cm^{-1} are compared with the experimental result. Regarding the three low-energy peaks of the calculated spectrum, the barrier height has no influence on the intensity but it influences the location of the peak. In this case, a higher barrier height is responsible for higher force constants and consequently for a higher HCCO term value of the main contributor (see below) to the corresponding peak. For the simulation using a barrier height of 981 cm^{-1} we obtain a good coincidence with the experimental peak C, whereas peak B' fits better in the simulation using a barrier height of 643 cm^{-1}. It is hard to decide which barrier height simulation is more congruent to the experiment. Due to the theoretical results summarized in Tables III and IV, which prefer uniquely a barrier height around 640 cm^{-1} as a reliable value, and because of the expected peak around 1250 cm^{-1} corresponding to the lowest-lying stretching fundamental (see Table VII) and to the peak C, from now on we only consider the third geometry and a barrier height of 643 cm^{-1} for HCCO.

Now, we will discuss the assignment which we obtain from the consideration of the bending part (Table VIII). The corresponding stick and Gaussian broadened spectra are presented in Fig. 6. In order to distinguish between theoretical and experimental peaks we introduce for the bending part of the theoretical spectrum a peak labeling $b=0,1,\ldots$ (in contrast to the labeling with uppercase letters for the experimental peaks) in energetical order. The main contributions for the eight lowest-lying peaks of the theoretical spectrum are considered in detail. Peak 0 represents a combination of five transitions between the lowest levels for different K quantum numbers. Peak 1 is made up of contributions arising from three transitions: Two of them lead from the lowest state for the quantum number $K^-=0$ to second and third level for the quantum number $K°=1$, respectively, the third transition correlates to the latter of the both, whereas the corresponding K quantum numbers are augmented by one. Peak 1 matches to the experimental peak B because both location and intensity are in good agreement. Peaks 2 and 3 are dominated by one transition from the lowest state for the quantum number $K^-=1$ to the seventh and tenth energy level, respectively, for the quantum number $K°=0$. Peak 2 shows a good coincidence in location with peak B' in the experimental spectrum but the corresponding intensity is too high in the simulation. For peak 3 no experimental counterpart could be found.

For the peaks 4 to 6, the number of appreciable contributors increases, whereas the intensity of the individual transitions decreases. Peaks four and five reflect the foothills on

TABLE VII. Relative one-dimensional Franck–Condon factors in the harmonic approximation for the transition $HCCO^-\rightarrow HCCO$. The Franck–Condon factors for the transition $(\nu_i^-=0)\rightarrow(\nu_i°=0)$ are set to unity. The given methods, basis sets, and frequencies refer to HCCO.

Method/ AO basis set	RCCSD(T)/DZP	UMP2/TZP (Ref. 10)	UHF-CCSD(T)/cc-pVTZ (Ref. 13)
		C–H coordinate, ν_1° progression	
Frequency ω_1°	3349	3372	3371
$\nu_1^-\rightarrow\nu_1^\circ$			
$0\rightarrow1$	0.006	0.000	0.000
$0\rightarrow2$	0.000	0.000	0.000
		O–C coordinate, ν_2° progression	
Frequency ω_2°	2050	2433	2099
$\nu_2^-\rightarrow\nu_2^\circ$			
$0\rightarrow1$	0.497	0.577	0.453
$0\rightarrow2$	0.117	0.210	0.102
$0\rightarrow3$	0.017	0.060	0.015
		C–C coordinate, ν_3° progression	
Frequency ω_3°	1240	1284	1249
$\nu_3^-\rightarrow\nu_3^\circ$			
$0\rightarrow1$	0.584	0.341	0.163
$0\rightarrow2$	0.164	0.060	0.012
$0\rightarrow3$	0.030	0.007	0.001

TABLE VIII. Assignment for bending part of the spectrum for the third geometry, a barrier height of 643 cm^{-1}, and a vibrational temperature of 200 K.

Peak label		Assigned transition					
				HCCO$^-$ state		HCCO state	
Theory	Experiment	Energy	Intensity	K^-	Level number i	$K°$	Level number i
		−267	0.070	2	1	1	1
		−130	0.226	1	1	0	1
0	A	−1	0.574	0	1	1	1
		10	0.311	1	1	2	1
		12	0.095	2	1	3	1
		418	0.086	0	1	1	2
1	B	457	0.174	0	1	1	3
		534	0.075	1	1	2	3
2	B'	893	0.101	1	1	0	7
3		1081	0.034	1	1	0	10
		1335	0.026	0	1	1	11
4		1349	0.026	0	1	1	12
		1394	0.021	0	1	1	13
		1458	0.052	0	1	1	14
5		1581	0.032	0	1	1	16
		1593	0.019	1	1	2	15
		1738	0.020	1	1	0	23
6	D	1758	0.035	1	1	2	20
		1846	0.019	1	1	0	25
7	E	2084	0.018	1	1	0	32

the high-energy side of the experimental peak C, and the peaks 6 and 7 contribute to the experimental peaks labeled as D and E. On the higher-energy side of peak 7, a few low-intensity features occur which will be called, from now on, the bending background.

For all stretching coordinates the Franck–Condon factors have been determined in a one-dimensional approach in order to simplify an assignment. In this case force constants for r_{OC} and r_{CC} have been readjusted to get the right frequency. For different calculations, the factors are summarized in Table VII.

Concerning the ν_1° progression, corresponding to the C–H stretching vibration, only the $(\nu_1^-=0)\rightarrow(\nu_1^\circ=0)$ transition has a nonvanishing intensity. Therefore, all the transitions with non-negligible contributions are characterized with $\nu_1^\circ=0$ for HCCO state. Thus, this quantum number is irrelevant for further considerations. The situation is different for the ν_2 and ν_3 quantum numbers corresponding to the out-of-phase and in-phase combination of the O–C and C–C stretching vibrations, respectively. The equilibrium distances of the anion compared with the neutral counterpart (Tables I and III) change so much that at least the $(\nu_i^-=0)\rightarrow(\nu_i^\circ=1)$ transitions $(i=2,3)$ get significant intensities.

Two-dimensional Franck–Condon factors with respect to the r_{OC} and r_{CC} coordinates have also been calculated.[37] In Table IX the two-dimensional data are compared with the one-dimensional approximation (by means of the relation $f_{OC,CC}=f_{OC}\cdot f_{CC}$ for the one-dimensional case), which leads to the conclusion that there is a considerable difference between the one- and two-dimensional treatments of the coordinates r_{OC} and r_{CC}. The calculations show that the Franck–Condon factors corresponding to transitions characterized by $(\nu_2^\circ=0,\nu_3^\circ>0)$ decrease appreciably, while the factors corresponding to transitions characterized by $(\nu_2^\circ>0,\nu_3^\circ=0)$ increase slightly if the two-dimensional model is applied.

Now, we consider the influence of the stretching vibrations. For a short and concise assignment we introduce the triples $(\nu_2^\circ,\nu_3^\circ;b)$ consisting of the stretching quantum numbers ν_2° and ν_3° and the labeling of the bending peaks b. In Fig. 7 the stretching modes are uncoupled (one-dimensional),

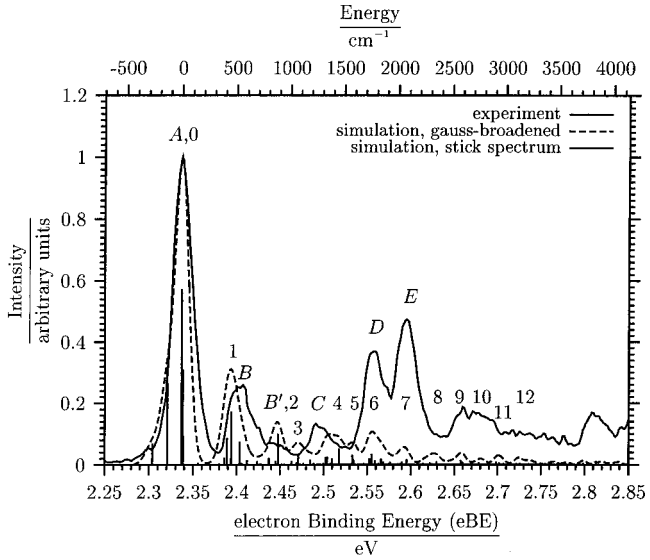

FIG. 6. For a barrier height of 643 cm^{-1} and the third geometry the simulated stick spectrum and the corresponding Gaussian-broadened spectrum are displayed along the low-energy range. Also the experimental spectrum is given in order to facilitate the assignment.

TABLE IX. Relative two-dimensional Franck–Condon factors in the harmonic approximation for the transition $HCCO^- \rightarrow HCCO$. The Franck–Condon factors for the transition $(\nu_2^- = 0, \nu_3^- = 0) \rightarrow (\nu_2^\circ = 0, \nu_3^\circ = 0)$ are set to unity.

Transition $\nu_2^-, \nu_3^- \rightarrow \nu_2^\circ, \nu_3^\circ$	Frequency cm^{-1}	UHF-CCSD(T)/cc-pVTZ (Ref. 13)	
		One-dimensional	Two-dimensional
0,0→0,1	1249	0.1627	0.0087
0,0→1,0	2099	0.4535	0.4721
0,0→0,2	2498	0.0121	0.0007
0,0→1,1	3348	0.0738	0.0007
0,0→0,3	3747	0.0005	0.0000
0,0→2,0	4198	0.1019	0.1293
0,0→1,2	4597	0.0055	0.0009
0,0→2,1	5497	0.0166	0.0029
0,0→3,0	6297	0.0151	0.0266

whereas in Fig. 8 O–C and C–C stretching coordinates are treated in the two-dimensional model. At first glance, the difference between the one and two-dimensional treatment, which is clearly reflected in Table IX, is concealed in the spectrum. But, in the case of a proper consideration it could be recognized again. In Fig. 7 an additional peak (labeled by the number $3'$) occurs. This is due to the non-negligible Franck–Condon factors for the transition to the (0,1;0) state in the lower-dimensional model. For the same reason a further peak arises at $3348\,cm^{-1}$ and is labeled by the number $12'$. It is assigned to the (1,1;0) state. As a secondary effect the intensity of the peaks 6 and 16 increases because of an additional contribution of the (0,1;1) and (1,1;1) state, respectively.

Now, the simulated spectrum which includes the two-dimensional model for the stretching vibrations (i.e., Fig. 8), is taken under consideration. The corresponding data are summarized in Table X. Since there is no contribution to the stretching vibration up to $1800\,cm^{-1}$ in this range no significant changes occur, as compared to Fig. 6. The peaks 6 and 7 in the latter figure are now represented by a superposition

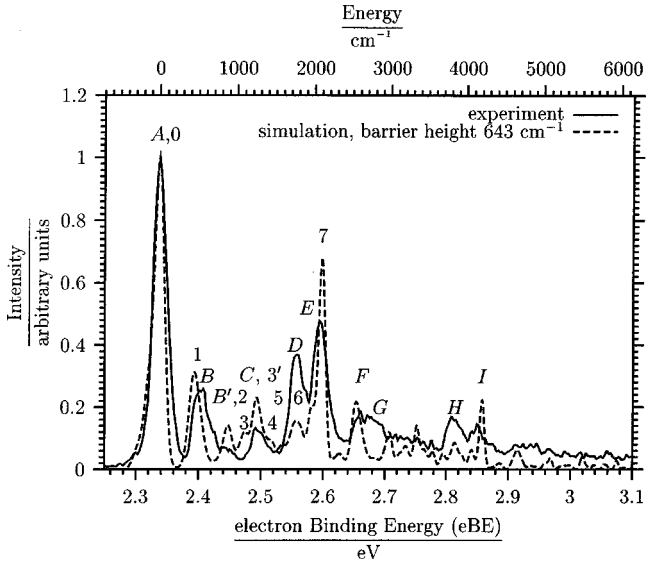

FIG. 7. Influence of the stretching modes is shown by comparison of the one-dimensional model with the experimental result.

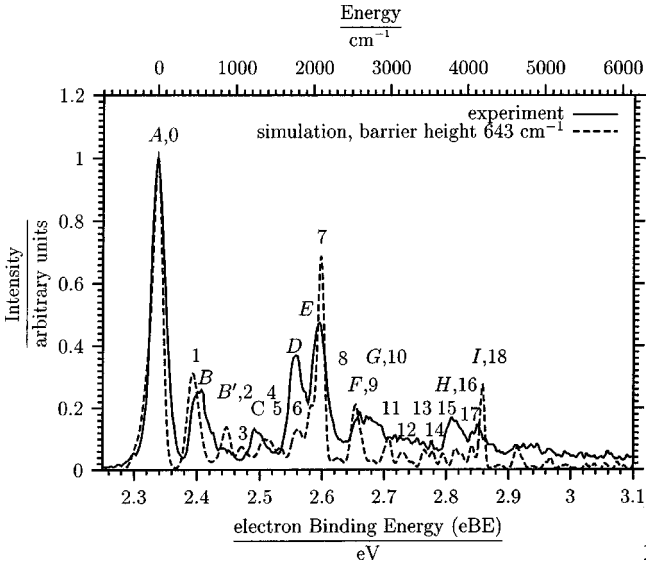

FIG. 8. The experimental spectrum is compared with the two-dimensional model for the stretching modes.

of the transitions into the states (0,0;6) and (0,0;7) with the transition into the state (1,0,0). The simulation overestimates the height of the experimental peak *E* by about a factor of 1.4. The following peaks up to $4200\,cm^{-1}$ represent a bending progression with origin at the (1,0;0) state superimposed on the bending background. So, peak 9 can be assigned to a combination of the transitions to the state (1,0;1) (bending progression) and the transition to the background state (0,0;9). Peak *F* can be regarded as the experimental counterpart. Both location and intensity are in good agreement. For the experimental peak *G* there hardly exists a theoretical correspondent. The simulation only offers the background state (0,0;10) (i.e., peak 10) with a very weak intensity. Under the following irregular structure up to peak *H* in the experimental spectrum, the peaks 11 to 15 can be found in the calculated spectrum. These peaks mainly represent the progression (1,0;2) up to (1,0;5). Only the peaks 11 and 12 are superimposed on the corresponding and more and more decreasing background bending states. The peaks 13 and 14 reflect the better resolution due to the corresponding energy range. Both belong to the same combination tone (1,0;4), but the resolution allows a splitting of the contributing components into the peaks 13 and 14. Peak 16 can be assigned to the state (1,0;6). The peak height is about a third of the value which was reached by the corresponding experimental peak *H*. For the peaks 17 and 18 the same is valid as for the peaks 13 and 14. Both can be assigned to the (2,0;0) state, which represents the origin of a following bending progression. Additionally, the state (1,0;7) contributes to peak 18. The experimental counterpart is peak *I*. Its peak height is overestimated by the simulation by 75%.

The intensity of the experimental peaks B', *E*, and *I* is significantly overestimated by the simulation. On the other side, underestimations occur with respect to the peaks *D*, *G*, and *H*. For a better reproduction of the experimental result, it is necessary to couple the bending and the stretching modes. This may enable an intensity transfer from peak 7 to peak 6.

TABLE X. Assignment $(\nu_2^\circ, \nu_3^\circ; b)$ for the stretching part of the spectrum for the third geometry, a barrier height of 643 cm^{-1}, and a vibrational temperature of 200 K. ν_2° and ν_3° denote the stretching quantum numbers and b labels the bending peaks.

Simulation			Assignment	Experiment		
Peak label	Term value	Peak height	$(\nu_2^\circ, \nu_3^\circ; b)$	Peak label	Term value	Peak height
6	1804	0.130	(0,0;6),(1,0;0)	*D*	1742	0.368
7	2100	0.686	(1,0;0),(0,0;7)	*E*	2057	0.474
8	2330	0.037	(0,0;8)			
9	2550	0.208	(1,0;1),(0,0;9)	*F*	2613	0.187
10	2776	0.030	(0,0;10)	*G*	2750	0.173
11	2982	0.105	(1,0;2),(0,0;11)			
12	3166	0.057	(1,0;3),(0,0;12)			
13	3448	0.064	(1,0;4)			
14	3556	0.058	(1,0;4)			
15	3690	0.052	(1,0;5)			
16	3853	0.069	(1,0;6)	*H*	3807	0.169
17	4067	0.078	(2,0;0)			
18	4200	0.272	(2,0;0),(1,0;7)	*I*	4121	0.146

Since the peaks 6 and 16 have the same bending labeling $(b=6)$, an intensity transfer would also be found for peak 16. In order to explain the lost intensity of peak *G*, one should remember that the lack of congruence of peak *B* and peak 1 propagates to the progression shifted by ω_2°. The assigned simulated peak (i.e., peak 10) stems from a background bending transition (0,0;10) and provides no explanation for this discrepancy.

A consideration of the dependence of the spectral shape from the temperature shows, that there occur competing mechanisms. For example, a rising temperature causes a lowering of peak 1 (the height of peak 0 is set to unity). On the other hand the second level for the K^- quantum number of $HCCO^-$ has to be taken into account and compensates the former. For this reason the regarded spectra are not sensitive to changes of the temperature at a magnitude of 50 K.

VI. CONCLUSION

In this paper we present the photoelectron spectrum of $HCCO^-$ at the photodetachment wavelength of 355 nm and its theoretical simulation. Most of the experimental peaks could be assigned to transitions into vibrational states of HCCO. Investigations of the low-energy range of the spectrum lead to a confinement of the deviation for the barrier height and equilibrium geometry of HCCO. Our analysis of the peak heights indicates that the structures of $HCCO^-$ and HCCO corresponding to the bending coordinates are closer to each other than suggested by the calculations which represent the basis for this work. By means of the location of the peaks, the barrier height of HCCO can be restricted to a value between 700 and 900 cm^{-1}. Considerations of the part of the spectrum which is dominated by the stretching vibrations show that there is a good agreement in the peak location, whereas the corresponding Franck–Condon factors seem to be too high for ν_2 and too low for ν_3. In a few domains of the spectrum, the simulation of the intensity profile underestimates the experimental result, which may be caused by the neglected couplings between bending and stretching motion. However, the spectrum could be assigned and this leads to an understanding of the photodetachment spectrum of $HCCO^-$.

ACKNOWLEDGMENTS

We want to thank Dr. B. Nestmann for useful discussions. The work is financially supported by the Deutsche Forschungsgemeinschaft (DFG) in the framework of the SFB 334. The experiments performed by D.M.N. and T.R.T. were supported by the Air Force Office for Scientific Research (No. F49620-00-1-0145).

[1] Y. Endo and E. Hirota, J. Chem. Phys. **86**, 4319 (1987).
[2] Y. Ohshima and Y. Endo, J. Mol. Spectrosc. **159**, 458 (1993).
[3] K. G. Unfried, G. P. Glass, and R. F. Curl, Chem. Phys. Lett. **177**, 33 (1991).
[4] K. G. Unfried and R. F. Curl, J. Mol. Spectrosc. **150**, 86 (1991).
[5] D. L. Osborn, D. H. Mordaunt, H. Choi, R. T. Bise, D. M. Neumark, and C. M. Rohlfing, J. Chem. Phys. **106**, 10087 (1997).
[6] L. R. Brock, B. Mischler, E. A. Rohlfing, R. T. Bise, and D. M. Neumark, J. Chem. Phys. **107**, 665 (1997).
[7] L. R. Brock, B. Mischler, and E. A. Rohlfing, J. Chem. Phys. **110**, 6773 (1999).
[8] J. M. Oakes, M. E. Jones, V. M. Bierbaum, and G. B. Ellison, J. Phys. Chem. **87**, 4810 (1983).
[9] J. D. Goddard, Chem. Phys. Lett. **154**, 387 (1989).
[10] K. Kim and I. Shavitt, unpublished results.
[11] M. T. Nguyen, W. Boullart, and J. Peeters, J. Phys. Chem. **98**, 8030 (1994).
[12] P. G. Szalay, J. F. Stanton, and R. J. Bartlett, Chem. Phys. Lett. **193**, 573 (1992).
[13] P. G. Szalay, G. Fogarasi, and L. Nemes, Chem. Phys. Lett. **263**, 91 (1996).
[14] B. Schäfer, M. Perić, and B. Engels, J. Chem. Phys. **110**, 7802 (1999).
[15] S. Seeger, *Ab initio Berechnungen an kleinen molekularen Anionen und Intermediaten in einfachen S_N2-Reaktionen*. Dissertation (Cuvillier, Göttingen, 1995).
[16] P. Botschwina and S. Schmatz, "Introduction and application of *ab initio* methods," in *The Structure, Energetics and Dynamics of Organic Ions*, edited by T. Baer, C. Y. Ng, and I. Powis (Wiley, New York, 1996), pp. 1–34.
[17] C. Xu, G. R. Burton, T. R. Taylor, and D. M. Neumark, J. Chem. Phys. **107**, 3428 (1997).
[18] R. B. Metz, A. Weaver, S. E. Bradforth, T. N. Kitsopoulos, and D. M. Neumark, J. Phys. Chem. **94**, 1377 (1990).

[19] D. L. Osborn, D. J. Leahy, D. R. Cyr, and D. M. Neumark, J. Chem. Phys. **104**, 5026 (1996).
[20] B. A. Mamyrin and D. V. Shmikk, Sov. Phys. JETP **49**, 762 (1979).
[21] G. Markovich, R. Giniger, M. Levin, and O. Cheshnovsky, J. Chem. Phys. **95**, 9416 (1991).
[22] J. Cooper and R. N. Zare, ''Photoelectron angular distributions,'' in *Lectures in Theoretical Physics*, edited by S. Geltman, K. T. Mahanthappa, and W. E. Brittin (Gordon and Breach, New York, 1969), pp. 317–337.
[23] MOLPRO98.1 is a package of *ab initio* programs written by H.-J. Werner and P. J. Knowles, with contributions from R. D. Amos *et al.*
[24] D. E. Woon and T. H. Dunning, Jr., J. Chem. Phys. **103**, 4572 (1995).
[25] R. A. Kendall, T. H. Dunning, Jr., and R. J. Harrison, J. Chem. Phys. **96**, 6796 (1992).
[26] P. J. Knowles, C. Hampel, and H.-J. Werner, J. Chem. Phys. **99**, 5219 (1993).
[27] P. J. Knowles, C. Hampel, and H.-J. Werner, J. Chem. Phys. **112**, 3106 (2000).
[28] M. Perić, B. Ostojić, B. Schäfer, and B. Engels, Chem. Phys. **225**, 63 (1997).
[29] P. R. Bunker and B. M. Landsberg, J. Mol. Spectrosc. **67**, 374 (1977).
[30] P. R. Bunker, B. M. Landsberg, and B. P. Winnewisser, J. Mol. Spectrosc. **74**, 9 (1979).
[31] H. Köppel, W. Domcke, and L. S. Cederbaum, Adv. Chem. Phys. **57**, 59 (1984).
[32] P. Botschwina, S. Seeger, M. Mladenović, B. Schulz, M. Horn, S. Schmatz, J. Flügge, and R. Oswald, Int. Rev. Phys. Chem. **14**, 169 (1995).
[33] M. Horn, M. Oswald, R. Oswald, and P. Botschwina, Ber. Bunsenges. Phys. Chem. **99**, 323 (1995).
[34] A. J. Merer and D. N. Travis, Can. J. Phys. **43**, 1795 (1965).
[35] R. N. Dixon, G. Duxbury, M. Horani, and J. Rostas, Mol. Phys. **22**, 977 (1971).
[36] B. Schäfer-Bung, ''Theoretische Untersuchung des Renner–Teller Effekts in asymmetrischen vieratomigen Molekülen,'' Dissertation, Universität Bonn, 2001.
[37] R. Berger, C. Fischer, and M. Klessinger, J. Phys. Chem. A **102**, 7157 (1998).